

Constructing a Uniform and Stable Mixed Conductive Layer to Stabilize the Solid-State Electrolyte/Li Interface by Cold Bonding at Mild Conditions

Yi Chen, Ji Qian, Xin Hu, Yitian Ma, Yu Li, Tianyang Xue, Tianyang Yu, Li Li, Feng Wu, and Renjie Chen**

Garnet-type $\text{Li}_{6.4}\text{La}_3\text{Zr}_{1.4}\text{Ta}_{0.6}\text{O}_{12}$ (LLZ) electrolyte is a promising candidate for high-performance solid-state batteries, while its applications are hindered by interfacial problems. Although the utilization of functional coatings and molten lithium (Li) effectively solves the LLZ interfacial compatibility problem with Li metal, it poses problems such as high cost, high danger, and structural damage. Herein, a mixed conductive layer (MCL) is introduced at the LLZ/Li interface (RT-MCL) via an *in situ* cold bonding process at room temperature. Such a stable and compact RT-MCL can effectively suppress side reactions and protect the crystal structure of LLZ, and it also inhibits growth of Li dendrites and promotes uniform Li deposition. The critical current density (CCD) of the Li symmetric cell composed of RT-MCL-LLZ is increased to 1.8 mA cm^{-2} and provides stable cycling performance over 2000 h under 0.5 mA cm^{-2} . Additionally, this *in situ* cold bonding treatment can significantly reduce cost and eliminate potential safety issues caused by the high-temperature processing of Li metal. This work highlights tremendous potential of this cold bonding technique in the reasonable design and optimization of the LLZ/Li interface.

1. Introduction

With the increasingly severe problem of global energy consumption, the development and utilization of new energy and

research on new energy storage devices have gradually become hot spots.^[1] As a battery system with mature technology and excellent performance, Li-ion batteries have been widely used in our daily life, including transportation, 3C products, and large-scale energy storage.^[2] However, the use of liquid electrolytes brings great safety hazards to Li-ion batteries.^[3] Using solid-state electrolytes (SSEs) instead of liquid electrolytes can reduce safety hazards and improve the safety of Li-ion batteries. Therefore, ASSBs are often considered to be the key to solving the safety problems of Li-ion batteries. In addition, it can be matched to the lithium (Li)-metal anode with a high theoretical specific capacity of 3860 mAh g^{-1} to increase the energy density of the battery,^[4] and Li-metal batteries are considered as the most promising next-generation batteries. However, the use of Li anodes is often accompanied by severe side reactions and the formation

of Li dendrites, leading to low coulombic efficiency and safety issues. It is often necessary to replace the liquid electrolyte with a SSE with the properties of non-flammability and high Young's modulus to alleviate the problems associated with the Li-metal anodes.^[5] Compared with polymer electrolytes, inorganic oxide-type SSEs possess higher ionic conductivities and wider electrochemical windows at room temperature.^[6] Specifically, the garnet-type $\text{Li}_{6.4}\text{La}_3\text{Zr}_{1.4}\text{Ta}_{0.6}\text{O}_{12}$ (LLZ) electrolyte is of particular fascination due to its excellent ionic conductivity ($\approx 10^{-4} \text{ S cm}^{-1}$ at room temperature), environmental-friendly handling, and good stability with Li metal.^[7] However, the poor Li wettability on the LLZ surface due to the non-lithium affinity of LLZ leads to poor solid contact and high interface resistance of LLZ/Li interface. In addition, the structural damage of LLZ caused by the side reaction between LLZ and Li metal and the cell short circuit caused by Li penetration through the LLZ will also occur during cycling (Figure 1a). These problems degrade the performance of LLZ and limit the application of LLZ electrolyte.^[8]

A variety of functional coatings were used to solve the contact problem existing at the LLZ/Li interface, and good interfacial wettability and interfacial contact were obtained.^[9] As a simple and feasible method, the Li affinity of the metal coating effectively improves the interface contact. The alloying reaction between the metal coating and Li improves the wettability

Y. Chen, J. Qian, X. Hu, Y. Li, T. Xue, T. Yu, L. Li, F. Wu, R. Chen
Beijing Key Laboratory of Environmental Science and Engineering
School of Materials Science and Engineering
Beijing Institute of Technology
Beijing 100081, China
E-mail: jiqian@bit.edu.cn; chenrj@bit.edu.cn

J. Qian, L. Li, F. Wu, R. Chen
Institute of Advanced Technology
Beijing Institute of Technology
Jinan, Shandong 250300, China

Y. Ma
School of Materials Science and Engineering
Xi'an University of Science and Technology
Xi'an 710054, China

L. Li, F. Wu, R. Chen
Collaborative Innovation Center of Electric Vehicles in Beijing
Beijing 100081, China

 The ORCID identification number(s) for the author(s) of this article can be found under <https://doi.org/10.1002/adma.202212096>.

DOI: 10.1002/adma.202212096

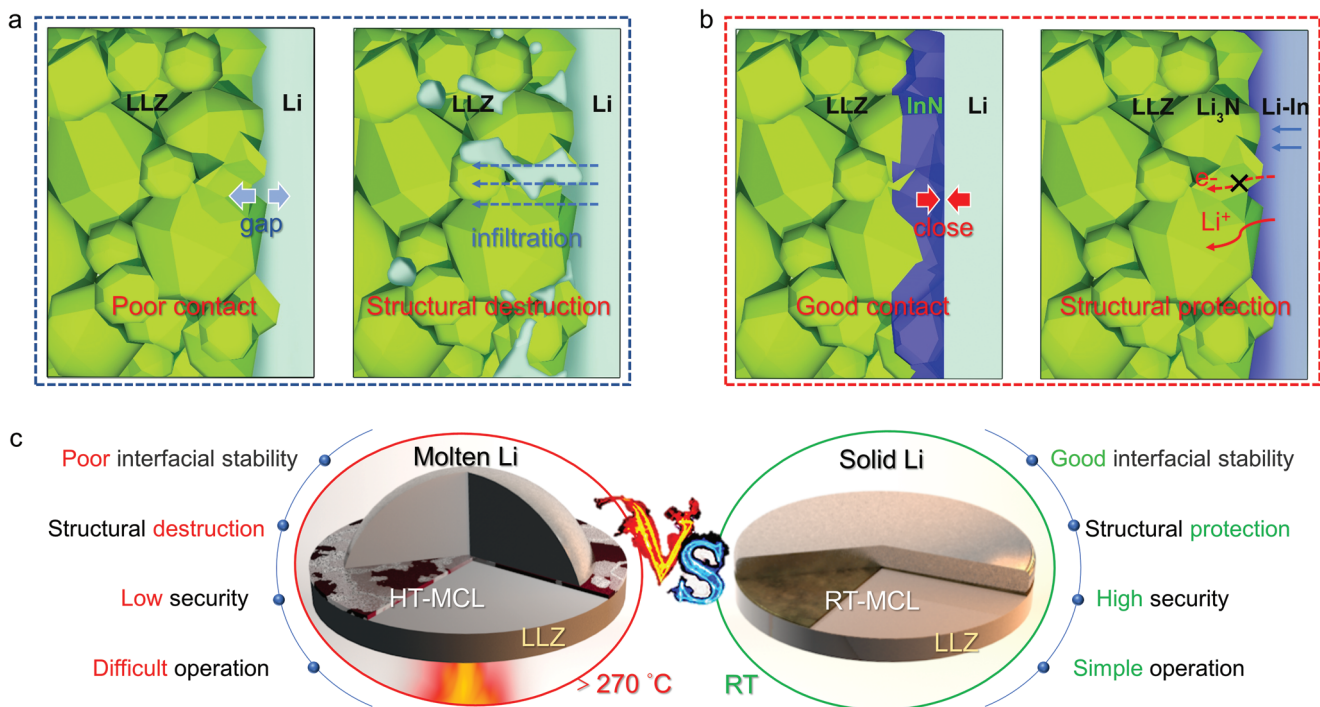


Figure 1. a,b) Schematic diagram illustrating the unmodified Li/LLZ interface (a) and Li/RT-MCL-LLZ interface (b), and c) the comparison between the HT-MCL-LLZ constructed by thermal bonding with molten Li (left) and the RT-MCL-LLZ constructed by cold bonding with solid Li (right) as the LLZ/Li interphases.

of Li on LLZ, greatly reducing the interface impedance and improving the interface stability during cycling.^[10] The formed alloy layer has been shown to be lithophilic and the LLZ/Li interface can provide a uniform Li-ion flux. A variety of metals, including Mg,^[11] Ge,^[12] Pt,^[13] Au,^[14] etc. have been used to form alloys to improve the LLZ/Li interface. However, the electronic conductivity provided by the alloy layer is usually high, easily triggering the side reactions between the LLZ electrolyte and Li metal, which is not conducive to hindering the growth of Li dendrites and protecting the structural integrity of LLZ electrolyte.^[15] The use of a doped alloy layer and a 3D alloy layer has a certain modification effect on addressing these problems, but it still cannot meet the expectations.^[16] Therefore, Sn_N,^[17] Sn_S,^[18] and other materials^[19] that can induce the formation of the mixed conductive layer (MCL) are proposed and widely used to improve LLZ/Li interface. The MCL has the characteristics of both an ionic conductive layer and an electronic conductive layer. The stable ionic conductive layer for Li metal can effectively protect the surface of Li metal and inhibit the crushing of Li metal. At the same time, the electron conductive layer with high Li⁺ diffusion coefficient can induce deposition of Li metal below the layer and protect the ion conductive layer so that the MCL can withstand large volume changes. As a result, MCL not only reduces the interface impedance, but also improves the long-term cycling stability of the LLZ/Li interface.^[20] However, in the preparation process as reported, high-temperature molten Li is always required to complete the thermal bonding process to form the MCL, which reduces the safety and operability and is not conducive to further commercial applications. Moreover, the damage of molten Li to the

structure of LLZ and the stability of the formed MCL also need to be considered.

In this work, we introduce a new strategy of cold bonding to construct the MCL as the LLZ/Li interphase. This new approach is based on the in situ conversion reaction between the pre-deposited InN layer and Li-metal anode at room temperature. The room temperature formed MCL (RT-MCL) not only improves the contact of the LLZ/Li interface, achieves uniform Li-ion flux distribution, and induces uniform Li deposition, but also reduces interfacial side reactions to stabilize the LLZ/Li interface and protects LLZ's bulk structure (Figure 1b). More importantly, this in situ cold bonding strategy can be realized to bond LLZ with Li at room temperature, avoiding the commonly used molten Li to form MCL at high temperature (HT-MCL).^[21] Compared with the use of molten Li, the use of solid Li at room temperature effectively eliminate the safety issues on handling Li at high temperature, improves the operability of sample preparation, reduces energy consumption, and makes outstanding contributions to maintaining interface stability and the structural integrity of LLZ (Figure 1c). The resulted CCD of RT-MCL-LLZ-based Li symmetric cells reaches as high as 1.8 mA cm⁻², and the cells show stable cycling performance and a small hysteresis voltage for over 2000 h at 0.5 mA cm⁻². The Li/RT-MCL-LLZ/LiFePO₄ full cells maintain a highly reversible capacity (> 160 mAh g⁻¹) after 100 cycles under 0.2C (1C = 170 mAh g⁻¹) at room temperature. These superior electrochemical properties suggest the significant effectiveness of RT-MCL constructed by cold bonding for optimizing the interfacial combability between LLZ electrolyte and Li-metal anode.

2. Results and Discussion

Dense LLZ pellets were obtained by ball milling and sintering of Al-doped LLZ powders (Figure S1, Supporting Information). Both the samples before and after sintering have similar diffraction patterns, belonging to cubic garnet phase $\text{Li}_5\text{La}_3\text{Nb}_2\text{O}_{12}$ (Figure S2, Supporting Information).^[22] The obtained LLZ pellets show a high ionic conductivity of $751 \times 10^{-4} \text{ S cm}^{-1}$ (Figure S3, Supporting Information) with an activation Energy (E_a) of 0.36 eV (Figure S4, Supporting Information) and the temperature dependence of the ionic conductivity can be well conformed to Arrhenius equation. The top-view scanning electron microscopy (SEM) image of pristine LLZ pellets presents that the LLZ pellets consist of primary crystals with distinct grain boundaries (Figure 2a). Uniform InN coating was obtained by magnetron sputtering (MS) in a nitrogen atmosphere. After MS treatment, the LLZ pellets are tightly covered by a dense and homogeneous InN layer with a thickness of $\approx 130 \text{ nm}$ (Figure 2b,c), accompanied by the color change on the surface of pellets from faint

white to bright yellow (Figure S5, Supporting Information). The flatness of the LLZ surface before and after sputtering can be observed by the atomic force microscopy (AFM). Compared with the LLZ surface (Figure S6, Supporting Information), the InN-LLZ surface is significantly smoother with greatly improved flatness (Figure 2d), which is also confirmed by SEM (Figure S7, Supporting Information). The top-view (Figure S8, Supporting Information) and cross-sectional (Figure 2e) SEM images and corresponding elemental mappings reveal that the thin but dense InN layer homogeneously covers the LLZ surface. Clear InN and LLZ interface can be observed by transmission electron microscopy (TEM), which confirms that the InN layer prepared by MS has good contact with LLZ (Figure 2f).^[23] In order to further characterize the InN coating, Raman spectroscopy and X-ray diffraction (XRD) measurements were used to analyze InN-LLZ. As the Raman spectra shown in Figure 2g, in addition to the peak of LLZ, the obvious InN peak is also detected on the surface of InN-LLZ.^[24] The XRD patterns in Figure 2h show that the diffraction peaks of LLZ and InN-LLZ

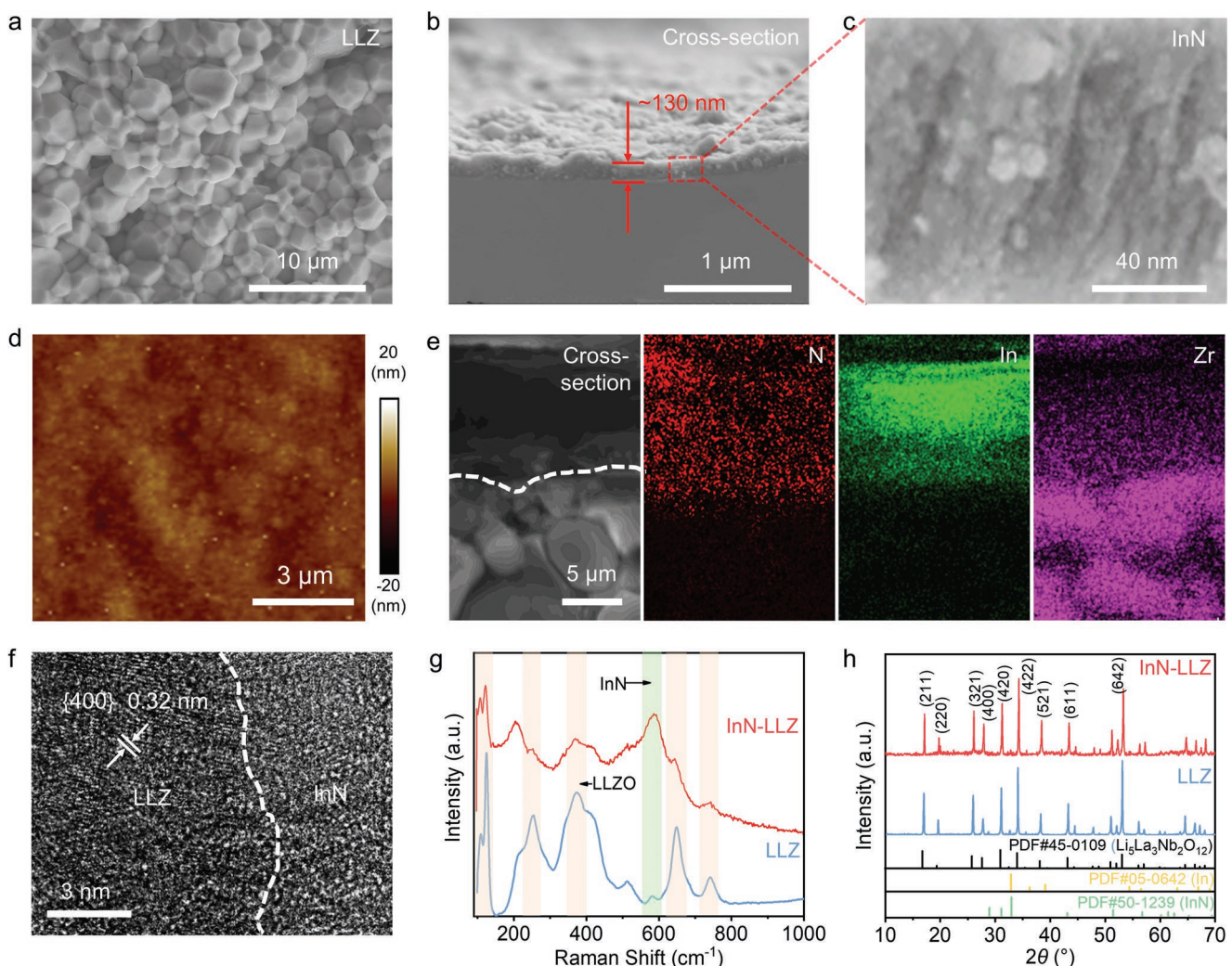


Figure 2. a) Top-view SEM image of pristine LLZ pellets. b,c) Cross-sectional SEM images of InN-LLZ (b) and partially enlarged view of the InN layer (c). d) AFM topography image of the InN-LLZ surface. e) Cross-sectional SEM image of InN-LLZ and the corresponding elemental mappings of N, In, and Zr. f) TEM image of InN-LLZ interface. g) Raman spectra of InN-LLZ and LLZ surfaces. h) XRD patterns of InN-LLZ and LLZ surfaces.

are in good agreement with the standard spectrum of the $\text{Li}_5\text{La}_3\text{Nb}_2\text{O}_{12}$ phase, and the corresponding InN peak can be found in the XRD pattern of InN-LLZ.^[24b] In summary, the target InN thin layers can be successfully constructed on the surface of LLZ pellets by MS methods, and the prepared InN layer has a dense structure, clear texture, flat surface, and good contact with LLZ, which is the precondition for preparing MCL with good performance.

To enable cold bonding at room temperature to prepare RT-MCL, the reaction energy values of a variety of common metal materials reacting with Li metal are calculated and compared (Table S1, Supporting Information). It is found that In possesses the most negative reaction energy among these metals reacting with Li, which indicates that In is more inclined to react with Li metal. Further, its nitride, i.e., InN, shows more negative reaction energy with Li due to its stronger oxidation capability compared to that of In, which makes the in situ conversion reaction between InN and Li metal more likely happen to facilitate the formation of MCL at room temperature (Figure 3a). In order to verify the above conclusion, we selected metals including the lithiophilic metals (Au, Zn, and In) and the lithiophobic metal (Fe), as well as InN to study their reaction capability with Li at room temperature (Figure S9, Supporting Information). This simple and mild cold bonding method to construct the RT-MCL on the LLZ/Li interface is illustrated in Figure 3b and the main procedures include modifying the LLZ surface with InN or metal thin layer via MS treatment, sticking Li foil on the modified LLZ surface, and then aging at room temperature for 2 days to implement the cold bonding process. During the aging process, certain kinds of the coating layer can react with Li metal to form the RT-MCL, while the others cannot. The reactions between different coating layers and Li metal during the aging process were studied by observing the color change of the LLZ surface and the adhesive attraction between Li metal and LLZ. After being stuck with Li metal and aged at room temperature for 2 days to ensure the full reaction between the coating layer and Li metal, the LLZ surface of low active metals (Au, Fe, and Zn) shows almost no change, while the color of the surface with In or InN changes from light brown to dark black (Figure 3c).^[25] In addition, the interface between Li metal and the LLZ with In or InN becomes tight and they are stuck together, which makes it difficult to tear off the Li metal (top in Figure 3d). The cross-sectional SEM image in Figure S10 (Supporting Information) indicates that LLZ is in close contact with Li metal and the RT-MCL interface has good integrity, which can further prove the strong adhesion between LLZ and Li metal. It is in sharp contrast to LLZ with other metals, which remain isolated from the Li metal after the aging process (bottom in Figure 3d).

To further prove the occurrence of the in situ room temperature conversion reaction between Li metal and InN layer on LLZ, the element distribution at the interface after the reaction was analyzed by XRD and energy-dispersive X-ray spectrum (EDS). Negative shift for the XRD peaks of Li metal after reacting with InN-LLZ is observed, which is due to the doping of In (Figure S11, Supporting Information). In addition, a large amount of In and N on the Li-metal surface after reaction are detected by EDS mapping, which proves that there is element migration at the RT-MCL-LLZ/Li interface (Figure 3e). To

further confirm the formed interphase after the in situ room temperature reaction, the cross-section of RT-MCL-LLZ/Li was analyzed by time-of-flight secondary-ion mass spectrometry (TOF-SIMS) 2D mapping and 3D distribution of related charged fragments (Figure S12, Supporting Information). It is found that a relatively dense Li_3N and a Li-In alloy layer with a diffusion tendency are produced at its interface (Figure 3f).^[26] In short, the InN thin layer on LLZ introduced by the MS method can react with Li metal to produce Li_3N and Li-In alloys at room temperature (Figure S13, Supporting Information). The reactions between InN and Li could be divided into two steps:^[27]



X-ray photoelectron spectroscopy (XPS) was used to analyze the composition changes on the LLZ surface after the cold bonding reaction. For comparison, the LLZ sample fabricated by reacting with the molten Li at a high temperature of 270 °C, a widely used and reported method to improve the LLZ/Li interface,^[15,28] was also prepared (Figure S14, Supporting Information) and denoted as HT-MCL-LLZ. The Li 1s XPS spectra in Figure 3g show that there are two typical peaks located at 55.2 and 55.9 eV after the reaction between InN and Li in both of these two samples, which are corresponding to the standard values of Li_3N and Li_2O , respectively. However, there is an additional peak of Li^0 in the spectrum of HT-MCL-LLZ, which may be caused by the destruction and penetration of MCL by molten Li, revealing that HT-MCL prepared by reacting with molten Li has poor homogeneity.^[29] For the In 3d XPS spectra in Figure 3h, the typical peaks of In shift to lower binding energy region to varying degrees, which may be due to the different enrichment of Li in the formed Li-In alloy.^[30] In the N 1s XPS spectra (Figure 3i), a peak located at ≈398.5 eV is observed for HT-MCL-LLZ and RT-MCL-LLZ, which can be attributed to the as-formed Li_3N . However, the peak of the original InN disappears for RT-MCL-LLZ, while it remains for HT-MCL-LLZ. It further proves that RT-MCL prepared by the in situ cold bonding method is more homogeneous, and high-temperature molten is not conducive to the stability and homogeneity of MCL.^[31] From the above results, we can confirm that the reaction between InN and Li is much more complete via the cold bonding method, and the RT-MCL constructed is rich in Li-In alloy, which can help stabilize the LLZ/Li interface and improve the cycling performance of the cell. Additionally, compared to the thermal bonding reaction constructing HT-MCL, the cold bonding reaction to construct RT-MCL will reduce the damage to the MCL and LLZ's structure, and avoids the potential short circuit problem due to the molten Li penetration, as shown in Figure S15 (Supporting Information).^[32]

The electrochemical performance of Li/RT-MCL-LLZ/Li symmetric cells and Li/RT-MCL-LLZ/LiFePO₄ full cells was evaluated to confirm the effects of in situ formed RT-MCL layer in improving the cell performance. Figure 4a shows the schematics illustrating the configuration of the Li symmetric cell (left) and full cell (right) assembled with RT-MCL-LLZ. Critical current density (CCD) measurements were first performed on the Li symmetric cells with the LLZ, In-LLZ, and RT-MCL-LLZ

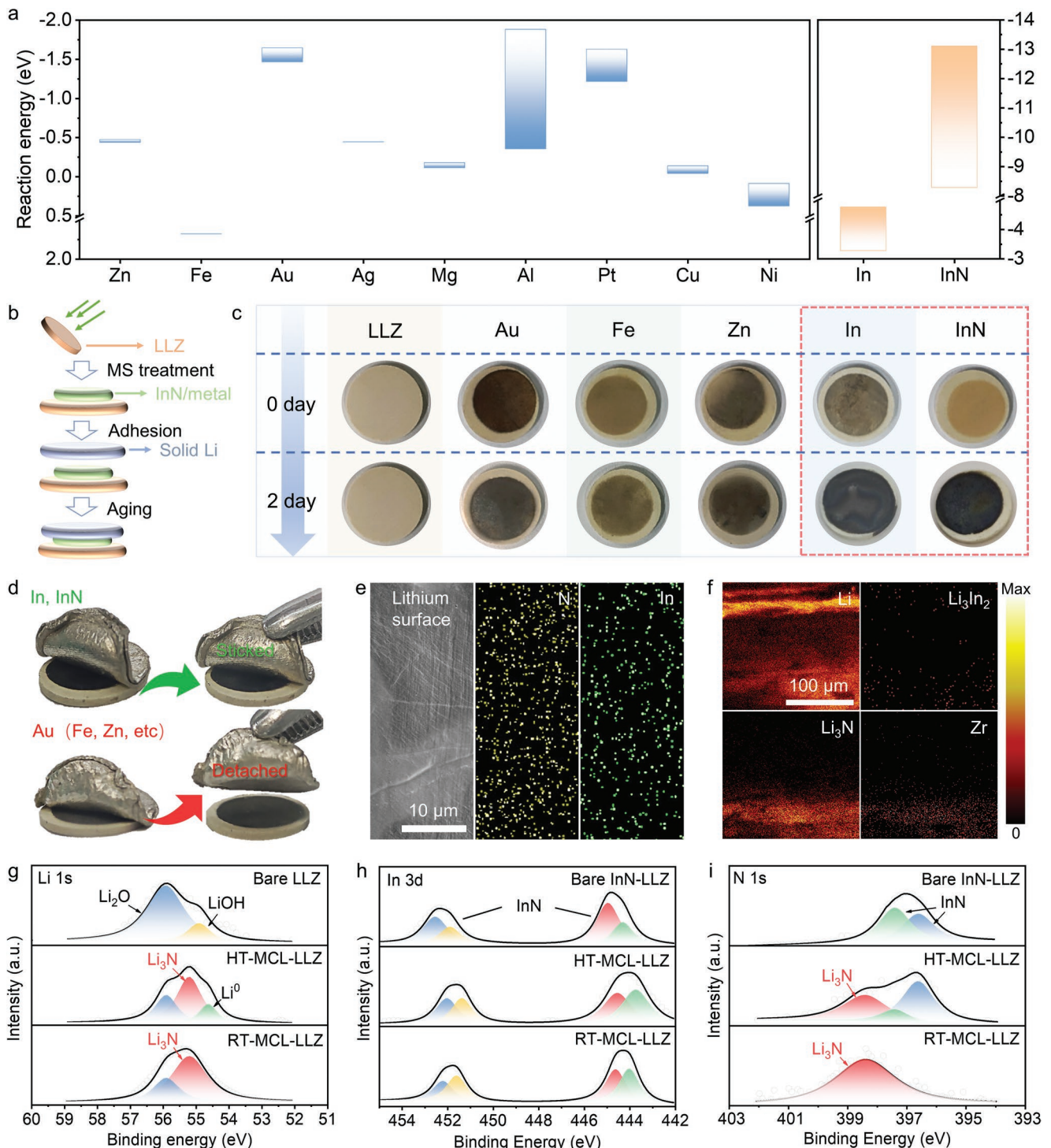


Figure 3. a) The calculated reaction energy of the reaction between Li and various materials. b) Schematic illustrating the cold bonding method conducted at room temperature. c) Photos showing the color changes of LLZ with different interfacial layers reacting with Li metal at room temperature. d) Photos showing the adhesion attraction of the modified LLZ and Li metal after cold bonding reaction. e) EDS spectrum and f) TOF-SIMS 2D mapping of the Li-metal surface after cold bonding reaction. g–i) XPS spectra in Li 1s (g), In 3d (h), and N 1s (i) regions of bare LLZ or InN-LLZ, HT-MCL-LLZ, and RT-MCL-LLZ.

electrolytes to evaluate their capability to suppress the Li dendrite. The corresponding voltage-time profiles of the cells with different electrolytes during the galvanostatic Li plating/stripping

cycling at stepwise increased current densities are shown in Figure 4b. The Li/RT-MCL-LLZ/Li cell can endure a high current density of 1.8 mA cm^{-2} without short circuit, which

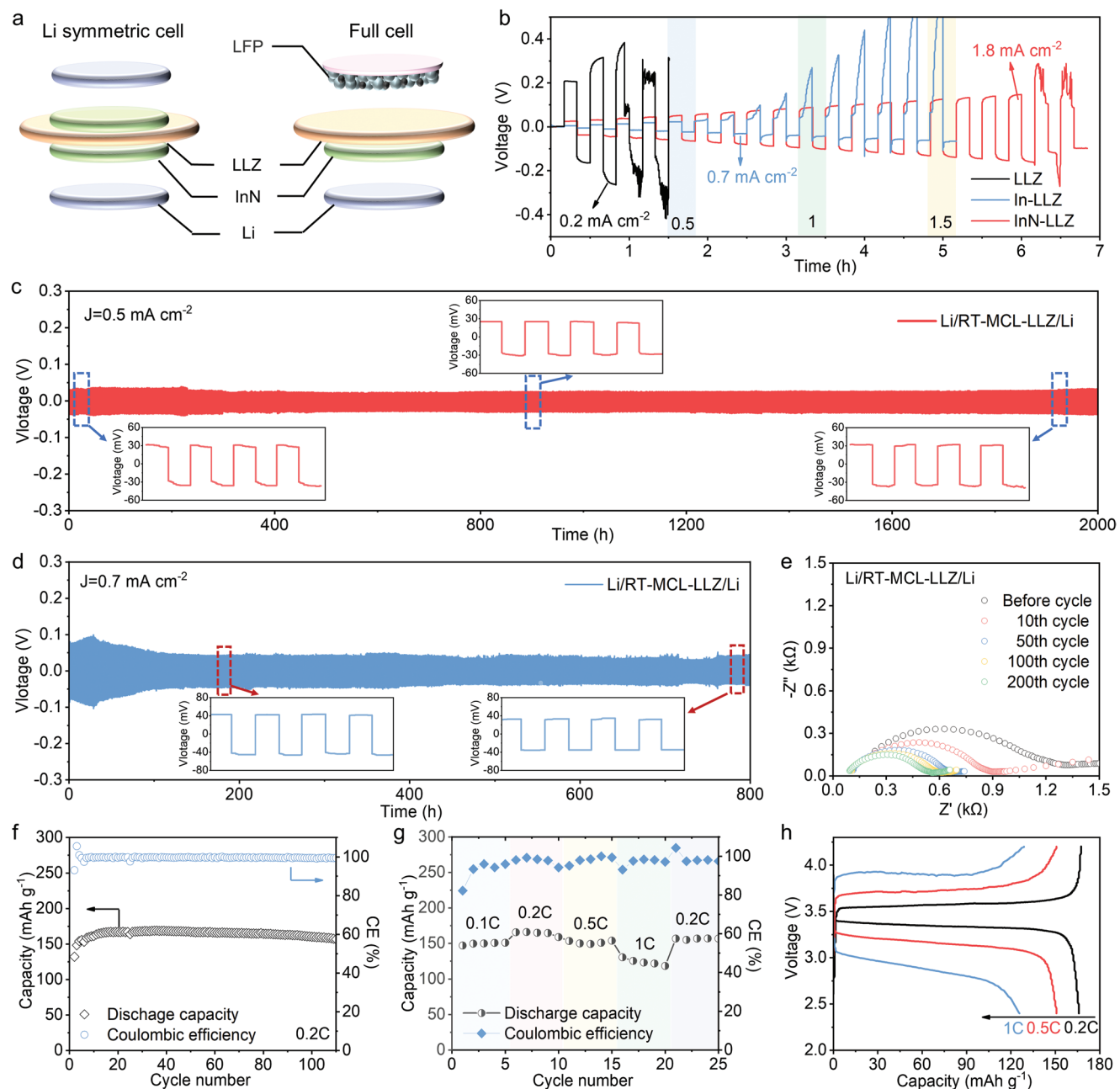


Figure 4. a) Schematics illustrating the configurations of Li/RT-MCL-LLZ/Li symmetric cell and Li/RT-MCL-LLZ/LiFePO₄ full cell. b) Voltage-time profiles of Li/LLZ/Li, Li/In-LLZ/Li, Li/RT-MCL-LLZ/Li cells during the galvanostatic Li plating/stripping cycling at stepwise increased current densities. c,d) Prolonged galvanostatic cycling performance of symmetric Li cells with RT-MCL-LLZ at 0.5 mA cm⁻² (c) and 0.7 mA cm⁻² (d). e) EIS curves of the Li/RT-MCL-LLZ/Li symmetric cell after different cycles at 0.5 mA cm⁻². f) Cycling performance of the solid-state Li/RT-MCL-LLZ/LiFePO₄ full cells at 0.2C (1C = 170 mAh g⁻¹). g) Rate capability and h) corresponding voltage-capacity profiles of the solid-state Li/RT-MCL-LLZ/LiFePO₄ full cells. The electrochemical measurements were performed at room temperature.

is far higher than 0.7 mA cm⁻² of In-LLZ and 0.2 mA cm⁻² of bare LLZ. The improved CCD reveals the functional RT-MCL interphase with effective dendrite suppression, which benefits from the effects that the well-formed MCL integrates the electronic conductive layer and the ionic conductive layer. In addition to improving the interface contact, the RT-MCL blocks the electrons from passing through the LLZ/Li interface and guides the horizontal deposition of Li by Li₃N with high surface

energy.^[33] The Li/HT-MCL-LLZ/Li cell was also measured for comparison (Figure S16, Supporting Information). The cell can endure a high current density of 1.2 mA cm⁻², which is still lower than RT-MCL-LLZ, and polarization increases rapidly under high current density. It is probably due to that, compared to the HT-MCL-LLZ, the RT-MCL-LLZ fabricated with the cold bonding method has a more uniform interface and a more enriched alloy layer, which provides a higher CCD and more

stable polarization potential.^[34] The galvanostatic cycling tests were further conducted to evaluate the cycling stability of the RT-MCL-LLZ/Li interface. The Li/RT-MCL-LLZ/Li symmetric cells could stably cycle as long as 2000 h at the current density of 0.5 mA cm^{-2} (Figure 4c). Even at a higher current density of 0.7 mA cm^{-2} , it can stably cycle for 800 h (Figure 4d). The enlarged voltage profiles present that the Li/RT-MCL-LLZ/Li symmetric cells possess flat voltage plating and stripping curves at 0.7 mA cm^{-2} with the overpotential of $\approx 50 \text{ mV}$ (see the insets in Figure 4d). This electrochemical performance is at the leading level in current research, showing the remarkable effects of RT-MCL in stabilizing the LLZ/Li interface (Table S2, Supporting Information). In contrast, the Li/HT-MCL-LLZ/Li cell fails within 30 h at a much lower current density of 0.1 mA cm^{-2} (Figure S17, Supporting Information), which is probably attributed to the fact that the molten Li penetrates the LLZ and even destroys the internal structure of LLZ, making the cell easier to be short-circuited. Moreover, the uneven Li deposition during the cycling in the case of inhomogeneous HT-MCL will accelerate the occurrence of short circuits. Additionally, the resistance of the Li/RT-MCL-LLZ/Li symmetric cell during cycling was evaluated with the electrochemical impedance spectroscopy (EIS) and the results shows that the resistance of the cell gradually decreases in the initial 50 cycles and then stabilizes (Figure 4e), proving the good stability of RT-MCL-LLZ/Li interface.

To further verify the contribution of RT-MCL to lowering the interfacial impedance and stabilize the interface between the LLZ and Li-metal anode, the electrochemical performance of the solid-state Li/RT-MCL-LLZ/LiFePO₄ full cell was further evaluated at room temperature. The Li/RT-MCL-LLZ/LiFePO₄ cell can deliver a specific capacity of 165.5 mAh g^{-1} at 0.2C ($1\text{C} = 170 \text{ mAh g}^{-1}$) and the capacity retention after 110 cycles remains as high as 92.4% (Figure 4f) with stable voltage polarization (Figure S18, Supporting Information), indicating the good stability of the RT-MCL interphase between LLZ and Li anode. Figure 4g,h shows the rate performance of the Li/RT-MCL-LLZ/LiFePO₄ full cell, which can deliver a discharge capacity of 153.9 mAh g^{-1} at 0.5C and 130.5 mAh g^{-1} at 1C without short circuit. In addition, the resistance of the Li/RT-MCL-LLZ/LiFePO₄ full cell remains at 300Ω after 50 cycles (Figure S19, Supporting Information). Thus, the Li/RT-MCL-LLZ/LiFePO₄ cell exhibits outstanding rate and cycling performance, which can be ascribed to the high-efficiency Li⁺ transportation at the stable RT-MCL interphase.

Multifarious analyses were conducted on the LLZ electrolyte and Li anode after cycling to achieve an in-depth understanding on the mechanism of RT-MCL stabilizing the LLZ/Li interface. The interfacial modification effect of the RT-MCL was first evaluated by SEM. The cells were disassembled after 50 cycles at 0.1 mA cm^{-2} and the cross-sectional SEM images in Figure S20 (Supporting Information) show the characteristics of intimate contact between RT-MCL-LLZ and Li-metal anode without obvious gap, while the gap exists between the bare LLZ and Li-metal anode, which confirms the role of RT-MCL in improving the contact between LLZ and Li metal. By studying the In-LLZ interface constructed by cold bonding after cycling, the penetration of Li into In-LLZ and the blurred interface can be clearly observed, proving that the use of In is less effective than that of

InN in preventing electron leakage between the Li-metal anode and LLZ and suppressing the growth of Li dendrites (Figure S21, Supporting Information). As shown in Figure 5a, a lot of messy Li dendrites are observed in the top-view SEM image (left) of the cycled LLZ, and obvious Li dendrite growth is also observed at the edge of LLZ in the cross-sectional SEM image (right), revealing the uneven Li plating/stripping at the LLZ/Li interface during cycling. The high electronic conductivity of LLZ is mostly responsible for Li dendrite formation in these SSEs,^[35] and it decreases after the RT-MCL modification (Figure S22, Supporting Information). Meanwhile, the formed Li-In alloy and Li₃N in RT-MCL are able to suppress the Li dendrite formation.^[27,36] As a result, the cycled RT-MCL-LLZ surface shows uniform and dense Li deposition without Li dendrites (Figure 5b). Figure 5c,d show the top-view SEM images of the Li-metal anode after cycling with LLZ and RT-MCL-LLZ electrolytes, respectively. In comparison with the Li dendrites and Li pulverization occurring on the Li-metal anode cycled with LLZ, the Li-metal anode cycled with RT-MCL-LLZ shows a much more compact and denser surface. The above results indicate that the formed RT-MCL interphase can effectively inhibit the formation of Li dendrites and guide the even Li plating and stripping.

In addition, after cycling, obvious holes and cracks can be observed on the LLZ particles in the cross-section SEM image of the bare LLZ pellet (Figure 5e), while the LLZ particles are maintained well with the RT-MCL (Figure 5f), suggesting that the RT-MCL can effectively protect the integrality of LLZ particles from severe damage during cycling.^[37] It has been reported that the LLZ/Li interface failure leads to huge interface impedance, the deterioration of the Li anode, and the destruction of the LLZ crystal structure.^[34,38] To confirm the well-maintained LLZ/Li interface with RT-MCL, the interfacial impedance of the Li symmetric cells with or without RT-MCL after cycling are obtained by EIS measurement (Figure 4e and Figure S23, Supporting Information) and then compared. As shown in Figure 5g, the resistance of Li/RT-MCL-LLZ/Li cell gradually decreases and then stabilizes. By contrast, the Li/LLZ/Li cell exhibits a much higher resistance and the resistance decreases in the initial 50 cycles and then increases, which may be due to the degradation of the LLZ/Li interface (as confirmed above) and the LLZ bulk structure. To verify the hypothesis on degraded LLZ structure, the crystal structure of LLZ after 200 cycles was studied by XRD and XPS characterizations. The results show that the peak width of bare LLZ is significantly larger and there are more stray peaks observed, indicating that the internal structure of LLZ is changed (Figure 5h). It is further confirmed by the Zr 3d XPS spectra in Figure 5i. The reduction of Zr can be clearly observed in bare LLZ after cycling, but not in RT-MCL-LLZ.^[39] Meanwhile, XPS results shown in Figure S24 (Supporting Information) confirm the existence of Li₃N and Li-In in both LLZ and Li surfaces, indicating the RT-MCL can be well maintained at the LLZ/Li interface even after long-term cycling. The above contents prove that RT-MCL not only has a good effect in inducing uniform Li deposition and inhibiting interface side reactions, but also is conducive to the protection of MCL and LLZ structures, so as to achieve a stable LLZ/Li interface.

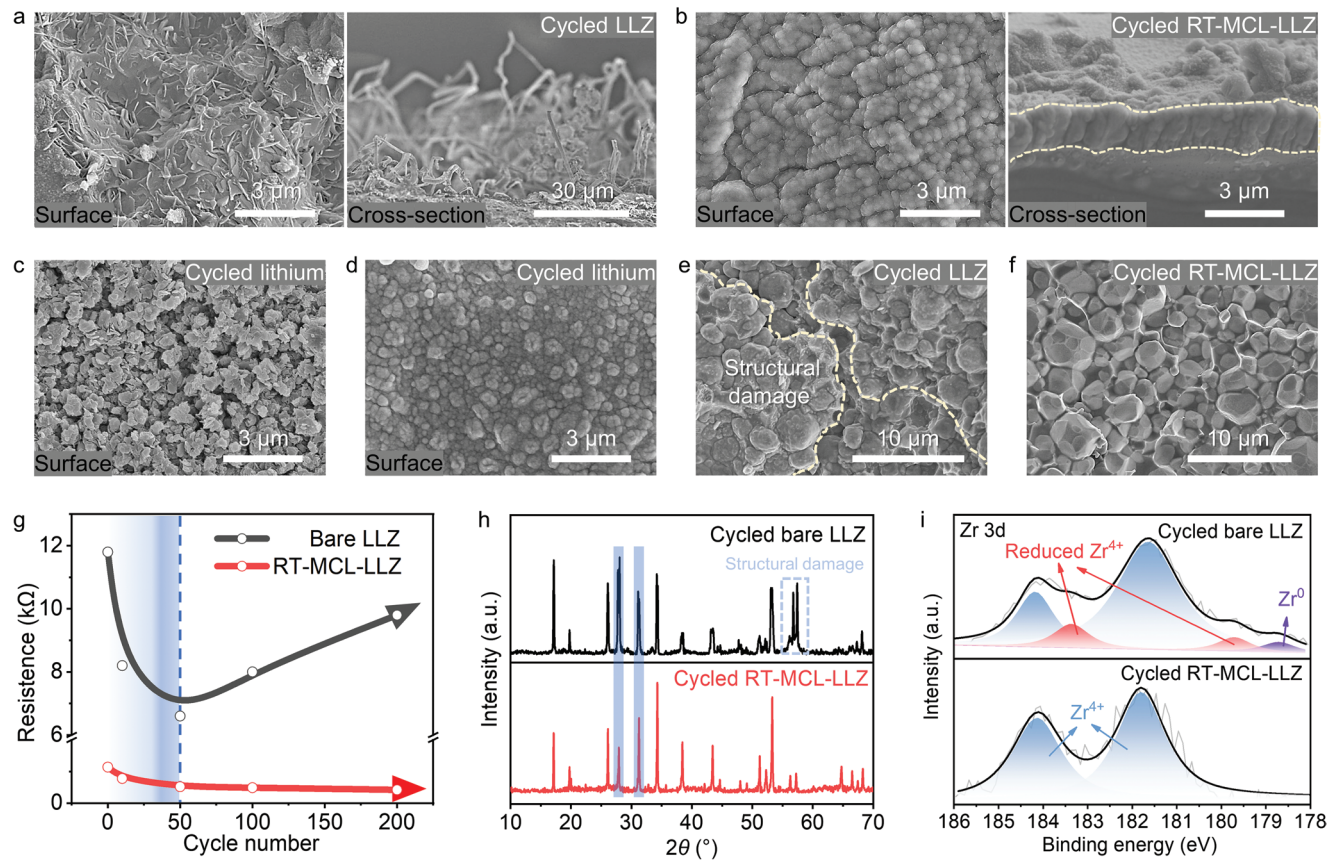


Figure 5. a,b) Top-view and cross-sectional SEM images of cycled LLZ (a) and RT-MCL-LLZ (b) electrolytes. c,d) Top-view SEM image of cycled Li-metal anodes stuck to LLZ (c) and RT-MCL-LLZ (d) electrolytes. e,f) Cross-sectional SEM images of cycled LLZ (e) and RT-MCL-LLZ (f) pellets. g) Resistance changes of Li/LLZ/Li and Li/RT-MCL-LLZ/Li cells in the initial 200 cycles. h) XRD patterns and i) XPS spectra in the Zr 3d region of LLZ and RT-MCL-LLZ after cycling.

3. Conclusion

A multifunctional RT-MCL interphase was constructed between the LLZ electrolyte and Li-metal anode by the room temperature cold bonding reaction between the InN coating layer and Li metal. The formed RT-MCL-LLZ/Li interface decreases the interfacial resistance, enables the homogenous but reversible Li plating/stripping, and suppresses the interfacial side reactions and Li penetration into LLZ. Moreover, the cold bonding preparation method greatly reduces the cost and effectively protects the LLZ/Li interface and the LLZ's structure. As a result, the RT-MCL-LLZ-based Li symmetric cell exhibits a CCD as high as 1.8 mA cm^{-2} and the cell delivers a stable cycling performance and a small hysteresis voltage for over 2000 h at 0.5 mA cm^{-2} . In addition, the Li/RT-MCL-LLZ/LiFePO₄ full cell maintains a highly reversible capacity above 160 mAh g^{-1} after 100 cycles at 0.2 C under room temperature. These superior electrochemical performances suggest the significant effectiveness of constructed RT-MCL by cold bonding method for optimizing the interfacial combability, which is verified by various analysis and testing methods on the cells with RT-MCL-LLZ after cycling. This cold bonding fabrication method shows great potential in constructing MCL for high-performance LLZ-based solid-state batteries. We believe that

this strategy can be extended to other types of solid-state batteries and energy storage applications.

4. Experimental Section

Synthesis of Garnet Solid-State Electrolytes: The cubic garnet electrolyte of Al-doped $\text{Li}_{6.4}\text{La}_3\text{Zr}_{1.4}\text{Ta}_{0.6}\text{O}_{12}$ (LLZ) composition was synthesized by conventional solid-state reaction. Stoichiometric amounts of LiOH (Meyer, 98.0%), La_2O_3 (Meyer, 99.9%), ZrO_2 (Meyer, 99.9%), Ta_2O_5 (Meyer, 99.5%), and Al_2O_3 (Meyer, 99.9%) were thoroughly ball milled in isopropanol for 24 h. 15 wt% excess LiOH was added to compensate for the vitalization of lithium (Li) during the subsequent calcination and sintering processes. The well-mixed precursors were dried and calcined at 920°C for 12 h. The resulting powder was ball milled in isopropanol for 48 h. The dried powders were pressed into 16 mm-diameter pellets at 300 MPa. The pellets were fully covered by the mother powder and sintered at 1050°C for 10 h. All the thermal processes were carried out in an alumina crucible and isolated from the air as much as possible. Before magnetron sputtering, the garnet electrolyte was mechanically polished on both sides to produce clean and flat surfaces.

Preparation of InN-LLZ and Metal-LLZ: The InN coating layer was performed via radio-frequency (R.F.) magnetron sputtering with a pure In target in a N_2 atmosphere, and the sputtering parameters were optimized to distance from target to substrate of 7 cm, power of 80 W, time of 10 min, and pressure of 1.0 Pa. The deposition of other metal coating layers was performed via R.F. magnetron sputtering with pure

metal targets in an Ar atmosphere, and the sputtering parameters were optimized to distance of 7 cm from target to substrate, power of 30 W, time of 10 min, and pressure of 1.0 Pa.

In Situ Construction of MCL: The RT-MCL was constructed on LLZ by the cold bonding method. In detail, the Li-metal anode was stuck to the surface of InN-LLZ in an argon-filled glove box, and then aged at room temperature for 2 days to make the InN layer completely react with Li metal to form RT-MCL. The HT-MCL was constructed on LLZ by the thermal bonding method. The molten Li metal was dropped onto the surface of InN-LLZ in an argon-filled glove box to rapidly generate HT-MCL.

Preparation of LiFePO₄ Cathode: The LiFePO₄ cathode was prepared by mixing 80 wt% LiFePO₄, 10 wt% polyvinylidene fluoride (PVDF), and 10 wt% superP in N-methylpyrrolidone. The active material loading of the as-prepared electrode was ≈2 mg cm⁻².

Symmetric Cell Assembly: To make Li/RT-MCL-LLZ/Li symmetric cells, the InN-LLZ pellet was sandwiched between two thin Li disks (≈1 cm in diameter and 450 μm in thickness) in an argon-filled glovebox. For the control sample, Li metal was applied with the same process to the surface-polished pristine LLZ pellet. For the solid-state Li/RT-MCL-LLZ/LiFePO₄ full cell, a Li disc was attached to an InN-LLZ pellet as electrolyte and anode. 5 μL of [EMIM][TFSI] was dropped between the cathode and LLZ electrolyte. The cells with the InN-LLZ pellets were stored at room temperature for 2 days prior to the electrochemical measurements.

Material Characterization: Morphology investigations were performed using a transmission electron microscope (FEI Talos F200X) and scanning electron microscope (Hitachi S-4800). AFM (Bruker, Dimension Icon, US) was also used to observe the morphology of LLZ surface. XRD patterns were recorded on an X-ray diffractometer (Rigaku Ultima IV-185) with Cu-Kα radiation ($\lambda = 0.154$ nm). The Raman spectra were obtained using a DXR Raman microscope with an excitation length of 532 nm. The X-ray photoelectron spectroscopy (XPS) was carried out on a Thermo Escalab 250XI spectrometer using a monochromatic Al K(alpha) X-ray source. TOF-SIMS (TOF-SIMS 5, ION TOF) was used to analyze the RT-MCL-LLZ cross-section chemical structure and for depth profiling.

Electrochemical Measurements: Electrochemical impedance spectroscopy (EIS) was performed on a CHI 660D workstation (Chenhua Instrument) with the frequency ranging from 1 MHz to 0.1 Hz and a voltage amplitude of 10 mV. To measure the LLZ's conductivity, Au was magnetron-sputtered on both sides of the LLZ pellets to prepare ion-blocking electrodes. The measurements for LLZ's electronic conductivity and ionic conductivity were both conducted on the Chenhua Instrument, CHI 660D workstation. The ionic conductivity was detected by the EIS method and then obtained by calculated with Equation (3), where σ_i is the ionic conductivity, L is the thickness of LLZ pellet, R_i is the resistance obtained from the EIS measurements, and S is the area of LLZ pellet. For electronic conductivity, the constant voltage of 1 V was applied and the response current was detected. The corresponding results of electronic conductivity were obtained by Equation (4), where σ_e is the electronic conductivity, L is the thickness of LLZ pellet, R_e is the resistance, S is the area of InN-LLZ pellet, I is the response current, and U is the constant voltage.

$$\sigma_i = \frac{L}{R_i S} \quad (3)$$

$$\sigma_e = \frac{L}{R_e S} = \frac{LI}{US} \quad (4)$$

The critical current density (CCD) was measured by galvanostatic cycling from 0.1 to 2.5 mA cm⁻² with increasing current at intervals of 0.1 mA cm⁻², and the duration of each cycling step was 10 min. All symmetric Li stability data were tested in time constant mode. All the galvanostatic cycling tests on the Li symmetric cell and the Li/RT-MCL-LLZ/LiFePO₄ cell were conducted on a Land 2001A battery testing system. The full cell was charged and discharged between 2.4 and 4.2 V. All the electrochemical tests were carried out at room temperature.

Supporting Information

Supporting Information is available from the Wiley Online Library or from the author.

Acknowledgements

This work was supported by the National Natural Science Foundation of China (52002024), National Key R&D Program of China (2021YFB3800300), Beijing Outstanding Young Scientists Program (BJJWZYJH01201910007023), Young Elite Scientists Sponsorship Program by CAST, Xiaomi Innovation Joint Fund of Beijing Municipal Natural Science Foundation (L223012), and Key Technology Research and Development Program of Shandong (2022CXGC020301).

Conflict of Interest

The authors declare no conflict of interest.

Data Availability Statement

The data that support the findings of this study are available from the corresponding author upon reasonable request.

Keywords

cold bonding, garnet electrolyte, interfacial modification, RT-MCL, solid-state Li-metal batteries

Received: December 25, 2022

Revised: February 6, 2023

Published online: March 25, 2023

- [1] J. B. Goodenough, Y. Kim, *Chem. Mater.* **2010**, 22, 587.
- [2] B. Jwa, Z. B. Dan, A. Cz, *Renew. Energy* **2020**, 162, 1629.
- [3] S. Li, M. Jiang, Y. Xie, H. Xu, J. Jia, J. Li, *Adv. Mater.* **2018**, 30, 1706375.
- [4] a) Y. Takeda, O. Yamamoto, N. Imanishi, *Electrochemistry* **2016**, 84, 210; b) J. Janek, W. G. Zeier, *Nat. Energy* **2016**, 1, 16141.
- [5] a) X.-Q. Zhang, X.-B. Cheng, Q. Zhang, *Adv. Mater. Interfaces* **2018**, 5, 1701097; b) X. Miao, H. Wang, R. Sun, C. Wang, Z. Zhang, Z. Li, L. Yin, *Energy Environ. Sci.* **2020**, 13, 3780; c) X. Song, C. Wang, J. Chen, S. Xin, D. Yuan, Y. Wang, K. Dong, L. Yang, G. Wang, H. Zhang, S. Zhang, *Adv. Funct.* **2022**, 32, 2108706.
- [6] a) R. Xu, X.-B. Cheng, C. Yan, X.-Q. Zhang, Y. Xiao, C.-Z. Zhao, J.-Q. Huang, Q. Zhang, *Matter* **2019**, 1, 317; b) R. Wang, L. Yang, J. Li, S. Pan, F. Zhang, H. Zhang, S. Zhang, *Nano Energy* **2023**, 108, 108174.
- [7] a) V. Thangadurai, S. Narayanan, D. Pinzar, *Chem. Soc. Rev.* **2014**, 43, 4714; b) L. Zhuang, X. Huang, Y. Lu, J. Tang, B. Tian, *Ceram. Int.* **2021**, 47, 22768; c) C.-L. Tsai, V. Roddatis, C. V. Chandran, Q. Ma, S. Uhlenbruck, M. Bram, P. Heitjans, O. Guillon, *ACS Appl. Mater. Interfaces* **2016**, 8, 10617.
- [8] L. Yang, Z. Lu, Y. Qin, C. Wu, C. Fu, Y. Gao, J. Liu, L. Jiang, Z. Du, Z. Xie, Z. Li, F. Kong, G. Yin, *J. Mater. Chem. A* **2021**, 9, 5952.
- [9] a) Z. Zhang, Y. Zhao, S. Chen, D. Xie, X. Yao, P. Cui, X. Xu, J. *Mater. Chem. A* **2017**, 5, 16984; b) W. Feng, J. Hu, G. Qian, Z. Xu, G. Zan, Y. Liu, F. Wang, C. Wang, Y. Xia, *Sci. Adv.* **2022**, 8, eadd8972;

- c) S. Lee, K. S. Lee, S. Kim, K. Yoon, S. Han, M. H. Lee, Y. Ko, J. H. Noh, W. Kim, K. Kang, *Sci. Adv.* **2022**, 8, eabq0153.
- [10] K. K. Fu, Y. Gong, B. Liu, Y. Zhu, S. Xu, Y. Yao, W. Luo, C. Wang, S. D. Lacey, J. Dai, Y. Chen, Y. Mo, E. Wachsman, L. Hu, *Sci. Adv.* **2017**, 3, e1601659.
- [11] K. (K.) Fu, Y. Gong, Z. Fu, H. Xie, Y. Yao, B. Liu, M. Carter, E. Wachsman, L. Hu, *Angew. Chem., Int. Ed.* **2017**, 56, 14942.
- [12] W. Luo, Y. Gong, Y. Zhu, Y. Li, Y. Yao, Y. Zhang, K. Fu, G. Pastel, C.-F. Lin, Y. Mo, E. D. Wachsman, L. Hu, *Adv. Mater.* **2017**, 29, 1606042.
- [13] Y.-K. Liao, Z. Tong, C.-C. Fang, S.-C. Liao, J.-M. Chen, R.-S. Liu, S.-F. Hu, *ACS Appl. Mater. Interfaces* **2021**, 13, 56181.
- [14] G. V. Alexander, S. Patra, S. V. Sobhan Raj, M. K. Sugumar, M. M. Ud Din, R. Murugan, *J. Power Sources* **2018**, 396, 764.
- [15] H. Huo, Y. Chen, R. Li, N. Zhao, J. Luo, J. G. Pereira da Silva, R. Mücke, P. Kagazchi, X. Guo, X. Sun, *Energy Environ. Sci.* **2020**, 13, 127.
- [16] a) X. He, F. Yan, M. Gao, Y. Shi, G. Ge, B. Shen, J. Zhai, *ACS Appl. Mater. Interfaces* **2021**, 13, 42212; b) Z. Wan, K. Shi, Y. Huang, L. Yang, Q. Yun, L. Chen, F. Ren, F. Kang, Y.-B. He, *J. Power Sources* **2021**, 505, 230062; c) W. Feng, X. Dong, Z. Lai, X. Zhang, Y. Wang, C. Wang, J. Luo, Y. Xia, *ACS Energy Lett.* **2019**, 4, 1725.
- [17] K. Shi, Z. Wan, L. Yang, Y. Zhang, Y. Huang, S. Su, H. Xia, K. Jiang, L. Shen, Y. Hu, S. Zhang, J. Yu, F. Ren, Y.-B. He, F. Kang, *Angew. Chem., Int. Ed.* **2020**, 59, 11784.
- [18] B. Zhao, W. Ma, B. Li, X. Hu, S. Lu, X. Liu, Y. Jiang, J. Zhang, *Nano Energy* **2022**, 91, 106643.
- [19] M. Cai, Y. Lu, L. Yao, J. Jin, Z. Wen, *Chem. Eng. J.* **2021**, 417, 129158.
- [20] X. Han, Y. Gong, K. (K.) Fu, X. He, G. T. Hitz, J. Dai, A. Pearse, B. Liu, H. Wang, G. Rubloff, Y. Mo, V. Thangadurai, E. D. Wachsman, L. Hu, *Nat. Mater.* **2017**, 16, 572.
- [21] F. Shen, M. B. Dixit, X. Xiao, K. B. Hatzell, *ACS Energy Lett.* **2018**, 3, 1056.
- [22] M. Cai, J. Jin, T. Xiu, Z. Song, M. E. Badding, Z. Wen, *Energy Storage. Mater.* **2022**, 47, 61.
- [23] C.-Y. Huang, Y.-T. Tseng, H.-Y. Lo, J.-K. Chang, W.-W. Wu, *Nano Energy* **2020**, 71, 104625.
- [24] a) C. Tessarek, S. Fladischer, C. Dieker, G. Sarau, B. Hoffmann, M. Bashouti, M. Göbel, M. Heilmann, M. Latzel, E. Butzen, S. Figge, A. Gust, K. Höflich, T. Feichtner, M. Büchele, K. Schwarzburg, E. Spiecker, S. Christiansen, *Nano Lett.* **2016**, 16, 3415; b) L. H. Abrha, T. T. Hagos, Y. Nikodimos, H. K. Bezabh, G. B. Berhe, T. M. Hagos, C.-J. Huang, W. A. Tegegne, S.-K. Jiang, H. H. Weldeyohannes, S.-H. Wu, W.-N. Su, B. J. Hwang, *ACS Appl. Mater. Interfaces* **2020**, 12, 25709.
- [25] K. Lee, S. Han, J. Lee, S. Lee, J. Kim, Y. Ko, S. Kim, K. Yoon, S. Jun-Hyuk, J. H. Noh, K. Kang, *ACS Energy Lett.* **2021**, 7, 381.
- [26] H. Zheng, S. Wu, R. Tian, Z. Xu, H. Zhu, H. Duan, H. Liu, *Adv. Funct. Mater.* **2020**, 30, 1906189.
- [27] Y. Ma, W. Qu, X. Hu, J. Qian, Y. Li, L. Li, H. Lu, H. Du, F. Wu, R. Chen, *ACS Appl. Mater. Interfaces* **2022**, 14, 44338.
- [28] K. Lee, S. Han, J. Lee, S. Lee, J. Kim, Y. Ko, S. Kim, K. Yoon, J.-H. Song, J. H. Noh, K. Kang, *ACS Energy Lett.* **2022**, 7, 381.
- [29] a) Z. Chen, W. Chen, H. Wang, C. Zhang, X. Qi, L. Qie, F. Wu, L. Wang, F. Yu, *Nano Energy* **2022**, 93, 106836; b) Y. Li, Y. Sun, A. Pei, K. Chen, A. Vailionis, Y. Li, G. Zheng, J. Sun, Y. Cui, *ACS Cent. Sci.* **2018**, 4, 97.
- [30] L. Zhang, X. Chen, F. Wan, Z. Niu, Y. Wang, Q. Zhang, J. Chen, *ACS Nano* **2018**, 12, 9578.
- [31] H. Xu, Y. Li, A. Zhou, N. Wu, S. Xin, Z. Li, J. B. Goodenough, *Nano Lett.* **2018**, 18, 7414.
- [32] H. Kitaura, E. Hosono, H. Zhou, *Energy Environ. Sci.* **2021**, 14, 4474.
- [33] a) Q. Pang, X. Liang, I. R. Kochetkov, P. Hartmann, L. F. Nazar, *Angew. Chem., Int. Ed.* **2018**, 57, 9795; b) K. Park, J. B. Goodenough, *Adv. Energy Mater.* **2017**, 7, 1700732.
- [34] X. He, X. Ji, B. Zhang, N. D. Rodrigo, S. Hou, K. Gaskell, T. Deng, H. Wan, S. Liu, J. Xu, B. Nan, B. L. Lucht, C. Wang, *ACS Energy Lett.* **2022**, 7, 131.
- [35] F. Han, A. S. Westover, J. Yue, X. Fan, F. Wang, M. Chi, D. N. Leonard, N. J. Dudney, H. Wang, C. Wang, *Nat. Energy* **2019**, 4, 187.
- [36] B. Wu, S. Wang, J. Lochala, D. Desrochers, B. Liu, W. Zhang, J. Yang, J. Xiao, *Energy Environ. Sci.* **2018**, 11, 1803.
- [37] X. Xu, Y. Liu, O. O. Kapitanova, Z. Song, J. Sun, S. Xiong, *Adv. Mater.* **2022**, 34, 2207232.
- [38] H. Huo, J. Liang, N. Zhao, X. Li, X. Lin, Y. Zhao, K. Adair, R. Li, X. Guo, X. Sun, *ACS Energy Lett.* **2020**, 5, 2156.
- [39] Y. Zhu, J. G. Connell, S. Tepavcevic, P. Zapol, R. Garcia-Mendez, N. J. Taylor, J. Sakamoto, B. J. Ingram, L. A. Curtiss, J. W. Freeland, D. D. Fong, N. M. Markovic, *Adv. Energy Mater.* **2019**, 9, 1803440.